Journal of Alloys and Compounds 1072 (2026) 188928

Contents lists available at ScienceDirect

Journal of Alloys and Compounds

journal homepage: www.elsevier.com/locate/jalcom

A novel synthesis pathway for oxide dispersion strengthened Fe−Cr alloys enabled by ultrasonic atomization

Sandipan Sen [a,*], Shubhashis Dixit [a], Marcel Muench [a,b], Liu Yang [a], Christoph Somsen [b], Sascha Seils [a], Daniel Schliephake [a], Alexander Kauffmann [b,*], Martin Heilmaier [a]

[a] Institute for Applied Materials (IAM-WK), Karlsruhe Institute of Technology (KIT), Engelbert-Arnold-Str. 4, Karlsruhe 76131, Germany
[b] Institute for Materials (IM), Ruhr University Bochum (RUB), Universitätsstr. 150, Bochum 44780, Germany

ARTICLE INFO

Keywords:
ODS steel
Ultrasonic atomization
Powder metallurgy
Dispersoids
Atom probe tomography

ABSTRACT

This study presents a novel powder metallurgical route for an oxide dispersion strengthened (ODS) ferritic Fe–14Cr–0.4Ti–0.5Y (wt%) alloy using ultrasonic atomization (UA) as an alternative to conventional mechanical alloying. The key novelty lies in exploiting residual O inherent to the elemental Y feedstock and process atmosphere as an internal oxidant, driving in-situ formation of $Y_{42}Ti_{10}O_{45}$ dispersoids directly from the liquid during atomization without utilizing Y_2O_3 powder. Diffusion length calculations and dispersoid spatial distributions confirm the liquid-phase nucleation and growth prior to matrix solidification. The dispersoids (20–100 nm) exhibit compositional stability during heat treatment at 1100 °C and field-assisted sintering at 1130 °C, though dispersoid density varies between powder particles due to non-uniform Y distribution in the melt pool. A microhardness of (282 ± 18) HV0.05 in high-dispersoid-density regions of consolidated samples is reached. This is comparable to mechanically alloyed counterparts, demonstrating UA as a promising alternative for ODS alloy fabrication.

1. Introduction

Fe-based oxide dispersion strengthened (ODS) alloys have been promising candidates for high temperature and nuclear applications. These alloys can be further subdivided into ferritic [1–4] and austenitic alloys [5,6]. Their use in fission and fusion reactor applications is attributed to their excellent swelling resistance, ability to reduce point defect concentration by trapping irradiation induced vacancies, and good irradiation creep resistance [1–4,7,8]. Additionally, they possess remarkable room temperature (RT) strength and excellent creep resistance above 600 °C [1,2,9–11]. The addition of Ti to the alloy composition promotes the formation of extremely fine Y–Ti–O nanoparticles, typically in the size range of 2–5 nm, in contrast to Ti-free ODS alloys, where the oxide dispersoids are coarser, ranging from 20 to 200 nm. These Y–Ti–O mixed oxides are commonly referred to as *nanoclusters* [10,12]. The dispersed nanoclusters effectively hinder dislocation motion by pinning dislocations [13,14], thereby enhancing strength, work hardening ability, high temperature creep resistance and eventually even ductility [11,15,16]. However, coarsening of these dispersoids reduces their effectiveness in hindering dislocation motion due to increased inter-dispersoid spacing [17,18]. Besides their direct impact on strengthening, they can also act as pinning centers for grain boundaries, thereby suppressing grain growth and resulting in ultrafine grains (compared to non-ODS counterparts), which contributes to Hall-Petch strengthening [12,13,16,19].

ODS alloys are usually manufactured via powder metallurgy routes, which include mechanical alloying (MA) as the crucial processing step [2,5,6]. For MA, high-energy ball milling of metal powders mixed with fine oxide particles (typically Y_2O_3) is utilized. The process involves repeated cold welding, fracturing, and rewelding of the metal powder particles, while the Y_2O_3 particles are simultaneously fragmented and dispersed throughout the matrix [20]. When Ti is present, Y-O-Ti clusters already form during milling and evolve further during consolidation through sequential enrichment in Ti and Y, ultimately forming thermally stable $Y_2Ti_2O_7$ nano-oxides at consolidation temperatures around 1100 °C [21]. These powders produced by MA are then typically consolidated via hot extrusion (HE) [22,23], hot isostatic pressing (HIP) [24,25], or field assisted sintering technique (FAST) [5,6,18,26]. Despite its widespread adoption for powder production [20,27–29], the MA route has some critical drawbacks, namely a substantial O and N pickup as well as

* Corresponding authors.
E-mail addresses: sandipan.sen@kit.edu (S. Sen), alexander.kauffmann@rub.de (A. Kauffmann).

https://doi.org/10.1016/j.jallcom.2026.188928
Received 24 March 2026; Received in revised form 15 May 2026; Accepted 27 May 2026
Available online 1 June 2026
0925-8388/© 2026 The Author(s). Published by Elsevier B.V. This is an open access article under the CC BY license (http://creativecommons.org/licenses/by/4.0/).

contamination by wear debris from milling balls and containers during ball milling [30,31]. Elevated O and N content can be potentially detrimental to ductility. For example, increasing the O content from 0.04 to 0.16 wt% in an Fe−22Cr−5Al ODS alloy promotes to the formation of stripe and chain precipitates near grain boundaries causing partial intergranular fracture and reduced ductility [32]. Inhomogeneous oxide distribution due to various processing related reasons is another drawback of the MA process, which negatively affects the mechanical properties in ODS Fe-Cr alloys [31,33].

To mitigate the drawbacks of classical MA routes, a novel synthesis route to produce ODS alloys is proposed in the present work. In this method, elemental Y is used to form dispersoids by oxidation instead of using Y_2O_3 powder in the production of the ODS alloy. Since most of the ferritic alloys described earlier are Fe-Cr based, with a Cr concentration between 13–14 wt%, the Cr content in the alloy studied here is set to 14 wt%. Ti is added to probe if this process can potentially form Y–Ti–O nanoclusters. ODS powders produced by MA typically contain 0.25–0.5 wt% Y_2O_3 [1–4]. We, therefore, set the Y content in the alloy to 0.5 wt% and the final composition is Fe−14Cr−0.4Ti−0.5Y (wt%), equivalent to Fe−15Cr−0.5–0.3Y (at%).

The study aims to answer the following research questions:

1. Is it thermodynamically and kinetically possible to form Y–Ti–O nanoclusters or dispersoids through internal oxidation of Y using ultrasonic atomization?
2. At which stage of the processing route do oxides form and what is their formation mechanism?
3. Do the dispersoids form uniformly with respect to chemical composition, size and spatial distribution?
4. How do the mechanical properties of ultrasonically atomized ODS alloys compare to mechanically alloyed counterparts from literature?

2. Materials and experimental methodology

2.1. Material synthesis

During the initial arc melting stage, two distinct synthesis approaches were employed to cast the alloy; one utilizing elemental Y and the other employing a Fe_2Y master alloy. This manuscript primarily focuses on the processing route involving elemental Y, while results for the Fe_2Y master alloy route (referred to as ODS-Fe_2Y) are provided in the Supplementary Material Figure S1.

The alloys were synthesized through repetitive arc melting on a water-cooled copper mold in an Ar (99.998% purity) atmosphere using an AM/0.5 furnace (Edmund Bühler GmbH, Germany). The purities of the constituents (Fe, Cr, Ti, and Y/Fe_2Y) were 99.95%. The arc-melted buttons were then drop cast into cylindrical rods of 10 mm diameter and 120 mm height in a water-cooled suction mold. The rods were further used for ultrasonic atomization (UA).

The UA process was carried out using an ATOLab+ (3DLab Ltd.) system. A schematic of the UA process is shown in Supplementary Material Figure S2. The chamber was evacuated till the O content in the chamber was about 10 ppm, then filled with Ar (99.998% purity). A crucible with steel inset was used. The machine was operated at a vibration frequency of 35 kHz, an amplitude of 60% and an arc current of 100 A (at arc light up) up to 165 A. The entire atomization process was carried out under continuously flowing Ar atmosphere (99.998% purity) with a flow rate of 25 l/min. The rods were systematically fed into the atomization chamber; a small part of the rod was then melted by an electric arc and deposited on the steel inset. The deposited material is maintained in a molten state using the movable arc. Further, the ultrasonic vibration is transferred from the cold end of the sonotrode towards the hot end, which forms capillary waves on the surface of the molten pool. Once the critical vibration amplitude is reached, the droplets were ejected to the flowing Ar stream, which cools them instantly and carried them to the cyclone chamber. Further details of the ATOLab+ device can be found in Ref. [34]. The powders were collected in a sealed chamber and transferred to a glove box all under Ar atmosphere.

To heat treat the atomized powder, a Mo foil envelope was created, the powder was then placed inside this Mo envelope. This powder-containing Mo envelope was then heat-treated at 1100 °C for 1 h in an HTRT 70–600/18 resistance tube furnace (Carbolite Gero GmbH & Co. KG, Germany), employing three evacuation-backfilling cycles followed by continuous Ar flow (99.998% purity) to minimize further oxidation. Atomized powder was also consolidated via FAST at 1100

and 1130 °C with an applied force of 24 kN and a dwell time of 5 min.

2.2. Compositional analysis

The composition of the drop cast rods, atomized and heat-treated powder as well as the FAST sample were obtained using inductively coupled plasma optical emission spectrometry (ICP-OES) for Fe, Cr, Ti, and Y. Similarly, carrier gas hot extraction (CGHE) was used to analyze O and N concentration. Furthermore, the O and N concentration of raw materials were measured using CGHE. At least five measurements were recorded for each condition to produce reasonable statistical data.

2.3. Microstructural characterization

The microstructural characterization of the alloy was carried out at distinct stages of the process. For scanning electron microscopy (SEM) investigation of the drop cast rod (cross-section view), the rods were sectioned using a diamond wire saw, ground with SiC abrasive sheets up to P4000 followed by polishing using 3 and 1 μm diamond suspension (5 min) and Buehler ITW (Germany) colloidal silica (10 min) on semi-automatic LaboPol-60 machine (Struers, Germany). The final polishing was carried out in a Vibromet machine (Buehler ITW, Germany) using a non-crystallizing oxide suspension (Struers, Germany) for 10 h.

The powders were first cold embedded mounted in a resin to obtain the cross-section specimen of the atomized and heat-treated powder (Epoclear, Schmitz-Metallographie GmbH, Germany). Once cured, the pellets were further hot embedded in EpoMet F (Buehler ITW, Germany). In the case of the consolidated sample, the specimens were cut using a diamond wire saw to obtain cross-sections. These pieces were then hot embedded like the powder samples. The final specimen preparation was carried out following the metallographic procedures analogous to those employed for the rods. Furthermore, the specimens for the top-view of powder were prepared by simply adhering the powder to a carbon tape.

Secondary electron (SEM-SE) and backscattered electron (SEM-BSE) contrast micrographs were obtained at an acceleration voltage of 20 kV using a Zeiss LEO 1530 scanning electron microscope (SEM, by Zeiss, Germany). Additionally, energy dispersive X-ray spectroscopy (SEM-EDS) of the rods, powder and consolidated specimens were obtained using a Zeiss Auriga 60 system operating at 20 kV with Octane Super-A detector (Ametek, USA).

Specimens for X-ray diffraction (XRD) analysis were prepared by mounting powder on a stub with resin, dried adequately, and polished to ensure a flat surface. The samples were then analyzed using a D2 Phaser device (Bruker Corp.) equipped with a Cu Kα source and a 1D LynxEye line detector. The XRD measurement was carried out over a span of 10–145° at a step size of 0.01° and the operating voltage and current of the source were kept at 30 kV and 10 mA. The accumulated acquisition time was 384 s per step.

Transmission electron microscopy (TEM) sample preparation was done with a Helios G4 focused ion beam (FIB)-SEM system by (ThermoFisher, USA). TEM investigations were conducted on a Tecnai F20 G2 SuperTwin microscope (ThermoFisher, USA) operated with a nominal acceleration voltage of 200 kV. High angle annular dark field images (HAADF) were obtained with a Fischione detector of type M3000 (E.A. Fischione Instruments, Inc., USA). Energy dispersive X-ray (STEM-EDS)

spectra were acquired with an EDAX detector of type Elite T Super with a sensor area of 70 mm^2 (Ametek, USA).

Atom probe tomography (APT) specimens were prepared directly from the powder samples using the conventional lift-out method using a FIB-SEM Strata 400S (ThermoFisher, USA). The APT measurements were conducted using a LEAP 4000X HR instrument (Cameca SAS) equipped with a UV laser operating at a wavelength of 355 nm. The experimental parameters were set to a specimen temperature of 50 K, a laser pulse energy of 50 pJ, a pulse frequency of 200 kHz, and a target detection rate between 0.3% and 1%. Three-dimensional reconstruction of the data was carried out with IVAS software version 3.6.14 (Cameca SAS), using SEM micrographs for guidance.

2.4. Microhardness tests

To evaluate the local mechanical properties of the alloys after sintering, microhardness measurements were performed on the FAST sample using a Qness Q10+ microhardness tester with a load of HV0.05. For each specific region, the hardness was determined by averaging the results of 20 individual indents.

3. Results

3.1. Impurity concentration of raw materials

Since the formation of oxide dispersoids via internal oxidation is being investigated in this study, it is of paramount importance that the impurity content in the alloys is tracked throughout the entire processing route, beginning with the raw materials. The O and N concentration of the raw materials are given in Table 1.

It is evident from Table 1 that the O content in Fe, Cr and Ti used is low (<0.02 wt%), while the elemental Y used in the study has a significantly higher concentration of O (0.823 wt%). N contamination is generally found to be negligible.

3.2. As-cast condition

To atomize the powders in the UA device, rods were drop cast (Supplementary Material Figure S2). To get a significant amount of powder at the end of the atomization process, four identically sized rods were drop cast. A schematic of the drop cast rods is shown in Fig. 1a. The microstructure and composition were carefully investigated for both ends (top and bottom) of each of the four rods to ensure compositional homogeneity prior to UA. This is crucial because there is a chance of elements with different densities (Fe: 7.87 g/cm^3, Cr: 7.19 g/cm^3, Y: 4.47 g/cm^3 and Ti: 4.54 g/cm^3 [35]) to separate during drop casting under the influence of gravity. This could cause compositional inhomogeneity in the rods which could be then carried over in the atomized powder.

The representative microstructure of the top and bottom section of one rod is also shown in Fig. 1a. SEM-BSE micrographs acquired from both sections of the rod reveal a microstructure characteristic of dendritic solidification. The microstructure is composed of a matrix with large grains that exhibits a darker contrast. A bright phase appears in interdendritic regions, both along the matrix grain boundaries and within the matrix grain interiors. The brighter contrast suggests an enrichment in elements with relatively high atomic number. As shown in the SEM-EDS elemental distribution map in Fig. 1b, these regions are indeed enriched in Y, while Fe, Cr, and Ti are uniformly distributed across the microstructure. The dendrites, in contrast, are depleted in Y but maintain a relatively uniform distribution of Fe, Cr, and Ti. The homogeneous presence of O further eliminates the possibility that the phase in the interdendritic regions is an oxide. The chemical compositions of Y-poor, dendrites and the Y-rich phase in the interdendritic regions, determined by standard-free SEM-EDS, are summarized in Table 2. Based on these observations, the intermetallic phase in the interdendritic regions possesses an Fe:Cr:Y atomic ratio of approximately 80:13:7.

Table 1
O and N content in the raw materials determined via CGHE.

Raw materials	O / wt%	N / wt%
Fe	0.0136 ± 0.0011	0.0003 ± 0.0010
Cr	0.0118 ± 0.0020	0.0003 ± 0.0001
Ti	0.0181 ± 0.0016	0.0022 ± 0.0002
Y	0.8230 ± 0.0420	0.0070 ± 0.0010

The crystal structures were investigated by X-ray diffraction (XRD) analysis performed on the rod samples. The XRD patterns confirmed the formation of the body-centered cubic (BCC) solid solution (W prototype, space group no. 229) corresponding to the matrix. The respective diffraction patterns are provided in Supplementary Material Figure S3. The volume fraction of the Y-enriched intermetallic phase appears too small to be detected by XRD. To further identify the crystal structure of the intermetallic phase, SEM-EBSD analyses were conducted in the Y-rich interdendritic regions. A representative Kikuchi diffraction pattern and its indexed solution are shown in Fig. 1c. The indexing result indicates the crystal structure of $Fe_{10}Cr_2Y$ ($ThMn_{12}$ prototype, space group no. 139).

The presence of a dendritic microstructure in the cast rods is not particularly concerning for the intended processing scheme, as the rods undergo remelting during the atomization process, wherein Y is fully miscible with both Fe and Cr in the liquid state. More importantly, the microstructure being consistent in the top and bottom sections of each rod indicates a high degree of chemical homogeneity. To further substantiate this observation, chemical analyses of samples collected from the top and bottom portions of all four rods are presented in Table 2.

It is seen from Table 2 that the overall alloy composition is close to the desired composition of Fe−14Cr−0.4Ti−0.5Y (wt%). The maximum deviation from the desired composition is observed for Fe (~2 wt%), relatively small deviations are observed for Cr (0.2 wt%) and Y (0.03 wt %) while almost no deviation can be observed for Ti. The O concentration across the top and bottom sections of all four rods is relatively uniform, ranging from 0.005 to 0.020 wt%. This slight variation can be expected since the four rods were cast in different casting experiments. Notably, the N concentration is low at this stage with the highest amount being 0.002 wt%. Comparing these values to the alloys produced by MA is not trivial, since these alloys are produced using Y_2O_3 powders. Only a few studies report O or N contents measured by CGHE, and even fewer additionally distinguish between O derived from the Y_2O_3 additions and excess O picked up during processing. García-Rodríguez et al. [36] isolated the excess O content by subtracting the stoichiometric O contribution of Y_2O_3. ODS Fe−14Cr−5Al-3W contained 0.297 wt% excess O and 0.220 wt% excess N, while ODS Fe−20Cr−5Al-3W showed lower levels of 0.104 wt% and 0.033 wt% of excess O and N, respectively. The comparison with the data obtained in the present study clearly shows that the impurity uptake during arc melting is significantly lower than that observed in mechanical alloying process.

3.3. Ultrasonic atomized and heat-treated powders

In this section, the morphology, microstructure and chemical composition of the powder samples produced by UA are presented. The results are categorized into two distinct powder conditions: the as-atomized state (AA), representing powder collected directly from the atomization process, and the heat-treated state (HT), referring to powder subjected to annealing at 1100 °C for 1 h. The heat treatment was performed to investigate one of two possible scenarios. In the first scenario, the heat treatment may facilitate nucleation and growth if the oxide dispersoids are not formed during atomization. In the second scenario, the heat treatment enables examination of possible changes in composition and size if such dispersoids are already present after

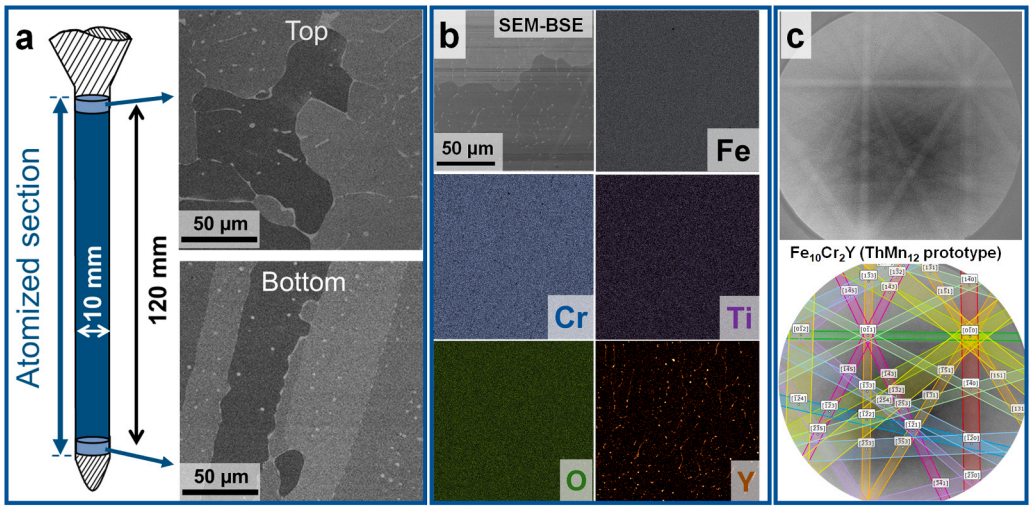

Fig. 1. a) Schematic of the drop cast rod along with SEM-BSE micrograph of the top and bottom section of the drop cast rod showing a dendritic microstructure. b) Representative SEM-EDS maps showing uniform distribution of Fe, Cr, Ti, and O. Y is found enriched in interdendritic regions. c) SEM-EBSD Kikuchi pattern of the Y-enriched phase in the interdendritic regions indicating the crystal structure of $Fe_{10}Cr_2Y$ ($ThMn_{12}$ prototype, space group no. 139).

Table 2
Chemical composition obtained by ICP-OES and CGHE from the top and the bottom of four rods after arc melting and drop casting. The desired composition is also added for comparison. The composition of the matrix and intermetallic dendritic arms (observed in Fig. 1a) obtained by SEM-EDS is also included.

Specimen condition		Average composition / wt%					
		Fe	Cr	Ti	Y	O	N
Desired		85.1	14	0.4	0.5	–	–
Rod 1	Top	84.1 ± 1.0	13.6 ± 0.2	0.4 ± 0.002	0.45 ± 0.01	0.004 ± 0.002	< 0.0005
	Bottom	84.3 ± 0.8	13.8 ± 0.3	0.40 ± 0.002	0.48 ± 0.01	0.005 ± 0.001	< 0.0005
Rod 2	Top	83.0 ± 0.1	13.9 ± 0.1	0.41 ± 0.004	0.45 ± 0.02	0.022 ± 0.002	0.002 ± 0.0007
	Bottom	82.7 ± 0.1	13.8 ± 0.1	0.40 ± 0.004	0.41 ± 0.02	0.007 ± 0.001	< 0.001
Rod 3	Top	82.8 ± 0.2	13.9 ± 0.1	0.40 ± 0.002	0.44 ± 0.02	0.015 ± 0.001	0.002 ± 0.0003
	Bottom	82.7 ± 0.4	13.8 ± 0.1	0.43 ± 0.005	0.51 ± 0.09	0.005 ± 0.003	< 0.001
Rod 4	Top	82.4 ± 0.1	13.8 ± 0.1	0.40 ± 0.001	0.53 ± 0.01	0.013 ± 0.001	< 0.001
	Bottom	82.6 ± 0.3	13.9 ± 0.1	0.40 ± 0.001	0.49 ± 0.01	0.005 ± 0.001	< 0.001
Avg.		83.1 ± 0.6	13.8 ± 0.1	0.39 ± 0.02	0.47 ± 0.02	0.009 ± 0.003	< 0.001
Dendrites (SEM-EDS)		85.2 ± 0.5	14.2 ± 0.1	0.36 ± 0.03	0.00 ± 0.10	–	–
Interdendritic regions (SEM-EDS)		80.9 ± 0.5	12.1 ± 0.1	0.42 ± 0.04	6.56 ± 0.10	–	–

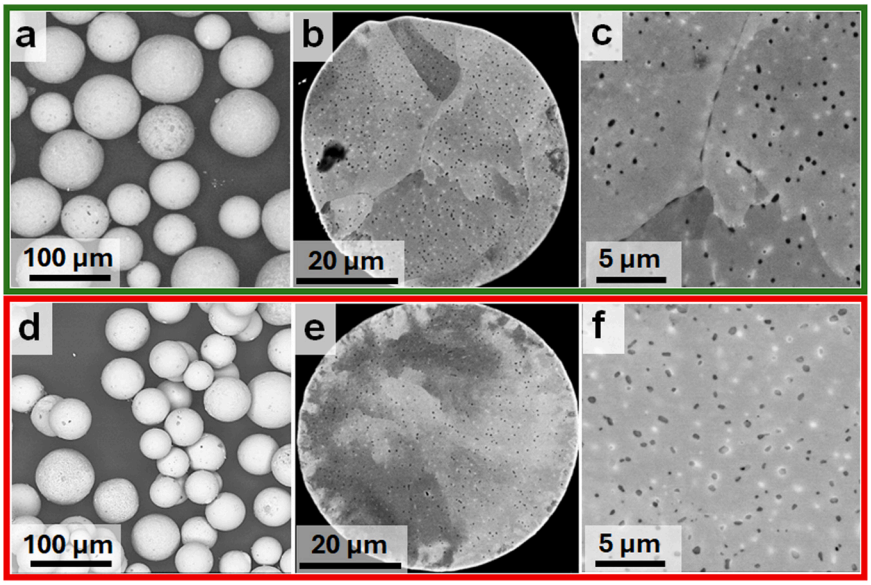

Fig. 2. SEM micrographs of: (a-c) AA powder and (d-f) HT powder. (a,c) Top view SE images, (b,e) BSE cross-section images, and (c,f) their magnified regions. The yellow and blue arrows highlight the dark and bright contrast dispersoids.

atomization.

Fig. 2a presents the top-view SEM-SE micrographs of the AA powder. The powder particles exhibit a predominantly spherical morphology with an average diameter of (59 ± 10) μm and a high sphericity of (0.90 ± 0.07). To investigate the microstructure of the powder particles, cross-sectional SEM-BSE micrographs were obtained, as shown in Fig. 2b–c. Two notable observations can be made: (i) The powder particles are dense and nearly pore-free. This is a clear advantage over gas atomization processes where hollow powder particles are common [37,38]. (ii) More importantly, the powder particles as shown for example in Fig. 2b–c contain uniformly distributed dispersoids throughout the SEM-BSE micrographs. These dispersoids, ranging from approximately 20–100 nm in size, are located both along grain boundaries and within the grain interior of the matrix. There are two types of dispersoids with respect to contrast – dark and bright, marked with yellow and blue arrows in Fig. 2c, respectively. The lower BSE contrast of the dispersoids suggests that they contain lighter elements, indicating a possible formation of an oxide or nitride phase. Based on the microstructural observations of the rods in Fig. 1, the bright phase is inferred to have a higher concentration of Y compared to the surrounding matrix and could potentially be a Y-rich intermetallic phase.

Fig. 2d presents the top-view SEM-SE micrographs of the HT powder particles. The powder particles appear partially agglomerated, which can be attributed to diffusion bonding occurring between adjacent particles during the heat treatment process. Fig. 2e–f display the microstructure of an individual HT powder particle. It is evident from these images that the type of dispersoids (dark and bright) observed in the AA condition are also present in the HT state, indicating a high degree of thermal stability of these dispersoids. The two types of dispersoids are marked in Fig. 2f with yellow (dark) and blue (bright) arrows like in Fig. 2c.

The dispersoids are, however, distributed non-uniformly across different powder particles in terms of their number, size, and spatial distribution. To categorize the powder particles, they are classified into three groups based on the dispersoid density within a given micrograph area as shown in Table 3. For statistical consistency, cross-section SEM-BSE images of 100 AA powder particles were analyzed at identical magnification (20,000 x) with an imaged area of 130 μm^2. The same reference area is used for the analysis of all SEM-BSE micrographs. The mean dispersoid radius, number of dispersoids, and volume fraction were calculated using ImageJ software. Based on the number density of dispersoids, the powder particles are grouped as follows: low density with $< 40 \bullet 10^2\ \mu m^{-2}$, medium density with $(40–200) \bullet 10^2\ \mu m^{-2}$, and high density with $> 200 \bullet 10^2\ \mu m^{-2}$. The dispersoid size was determined by considering at least 200 dispersoids for each of the three categories. The center-to-center distance of the dispersoids was calculated using the following relation [39]:

$$L = r\sqrt{\frac{32}{3\pi f}} \quad (1)$$

Where L is the center-to-center distance, r is the mean radius of the dispersoids, and f is the volume fraction of the dispersoids. The reported error represents the deviation obtained after analyzing multiple images of the same reference area of 130 μm^2.

Among the 100 analyzed powder particles, the majority exhibit medium dispersoid density (51% of the powder particles), followed by low (38%), and high dispersoid density particles forming the smallest fraction (10%). The center-to-center distance is the largest for powder particles with low dispersoid density and the smallest for those with high density. This trend is expected, as the dispersoids are homogeneously distributed within each individual powder particle. Notably, the average dispersoid size remains nearly identical across all three categories, strongly implying a similar dispersoid formation in all powder particles.

The chemical composition (determined by ICP-OES) of the atomized and heat-treated powder are shown in Table 4. Most notably, loss of around 0.2 wt% Y is recorded in the atomized powder with (0.30 ± 0.01) wt% compared to drop cast rods with (0.47 ± 0.02) wt%. The O content increased to (0.079 ± 0.001) wt% which indicates some pickup of O during the atomization process despite the < 10 ppm level O maintained in the Ar atmosphere during atomization. However, this content is still lower than O picked up during the MA process of several 0.1 wt% O as described in the previous section. Powder from the AA and HT conditions still show a ferritic (BCC) matrix. No peaks corresponding to the dispersoid phase are observed. The XRD results are shown in the Supplementary Material Figure S3.

To determine the chemical composition of the dispersoids, APT

Table 4
Chemical composition of AA and HT powder conditions obtained by ICP-OES and CGHE. The nominal composition has also been added for comparison.

Specimen Condition	Average composition / wt%					
	Fe	Cr	Ti	Y	O	N
Desired	85.1	14	0.4	0.5	-	-
AA	83.4 ± 0.2	13.2 ± 0.1	0.430 ± 0.004	0.290 ± 0.005	0.079 ± 0.001	0.003 ± 0.001
HT	84.7 ± 0.5	13.0 ± 0.1	0.410 ± 0.003	0.290 ± 0.002	0.102 ± 0.012	0.006 ± 0.001

Table 3
Quantitative microstructural data on AA powder particles classified based on dispersoid density: representative micrographs, average dispersoid size, center-to-center distance and dispersoid volume fraction. Additional representative SEM-BSE micrographs are also included.

Dispersoid number density ($100\ \mu m^{-2}$)	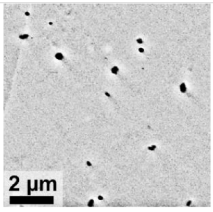 **Low (< 40)**	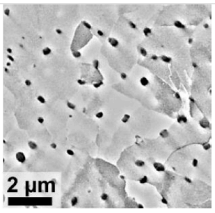 **Medium (40-200)**	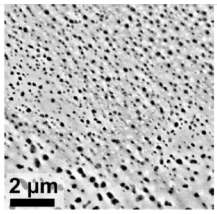 **High (> 200)**
Center-to-center distance (μm)	1.9 ± 0.7	0.9 ± 0.4	0.6 ± 0.3
Dispersoid size (nm)	100 ± 53	108 ± 65	101 ± 70
Dispersoid volume fraction (vol.%)	0.7 ± 0.2	4.2 ± 1.1	12.5 ± 2.4

samples were prepared from powder particles for the AA and HT condition. To maintain consistency, all the lift-outs for APT were done from powder particles with a medium dispersoid number density. Two tips, each of the AA and HT condition, are shown in Fig. 3.

Fig. 3a–b illustrate the APT results obtained from the AA powder, showing the spatial distribution of six elements: Fe, Cr, Ti, Y, O, and N. While Fe, Cr, and Ti exhibit relatively uniform distribution, noticeable inhomogeneity is evident for N, O, and Y. To further examine these regions of compositional variation, isosurfaces were constructed at 4 at% for Ti and 4 at% for N, as displayed in the enlarged view of Fig. 3a. For Fig. 3b, an isosurface for 9 at% Y was made, since no clear inhomogeneity was observed for Ti and N. Isosurfaces corresponding to a particular element delineate regions of high concentration of this particular element within the tip, revealing distinct interfaces between the element-rich regions and the surrounding matrix. These isosurfaces may represent either segregation, clusters or a secondary phase [40,41]. Segregation at grain boundaries, for example, generally spans a few nm with a spike in the concentration of one or a few elements. A cluster typically describes a small group of solute atoms detected as a local enrichment above the random matrix composition, often only a few nanometers or less in size, as is the case for the Y-Ti-O nanoclusters widely reported in ODS steel literature [10,12]. Secondary phases are, however, typically larger and often feature a sharp chemical interface to the matrix.

To quantify the composition of these features, a cylindrical region of interest (ROI) traversing each isosurface was defined, from which a one-dimensional (1D) concentration profile was extracted. Based on the size and compositional differences between the matrix and dispersoid observed in the 1D concentration profiles, the regions delineated by the isosurfaces can be confidently identified as dispersoids of secondary

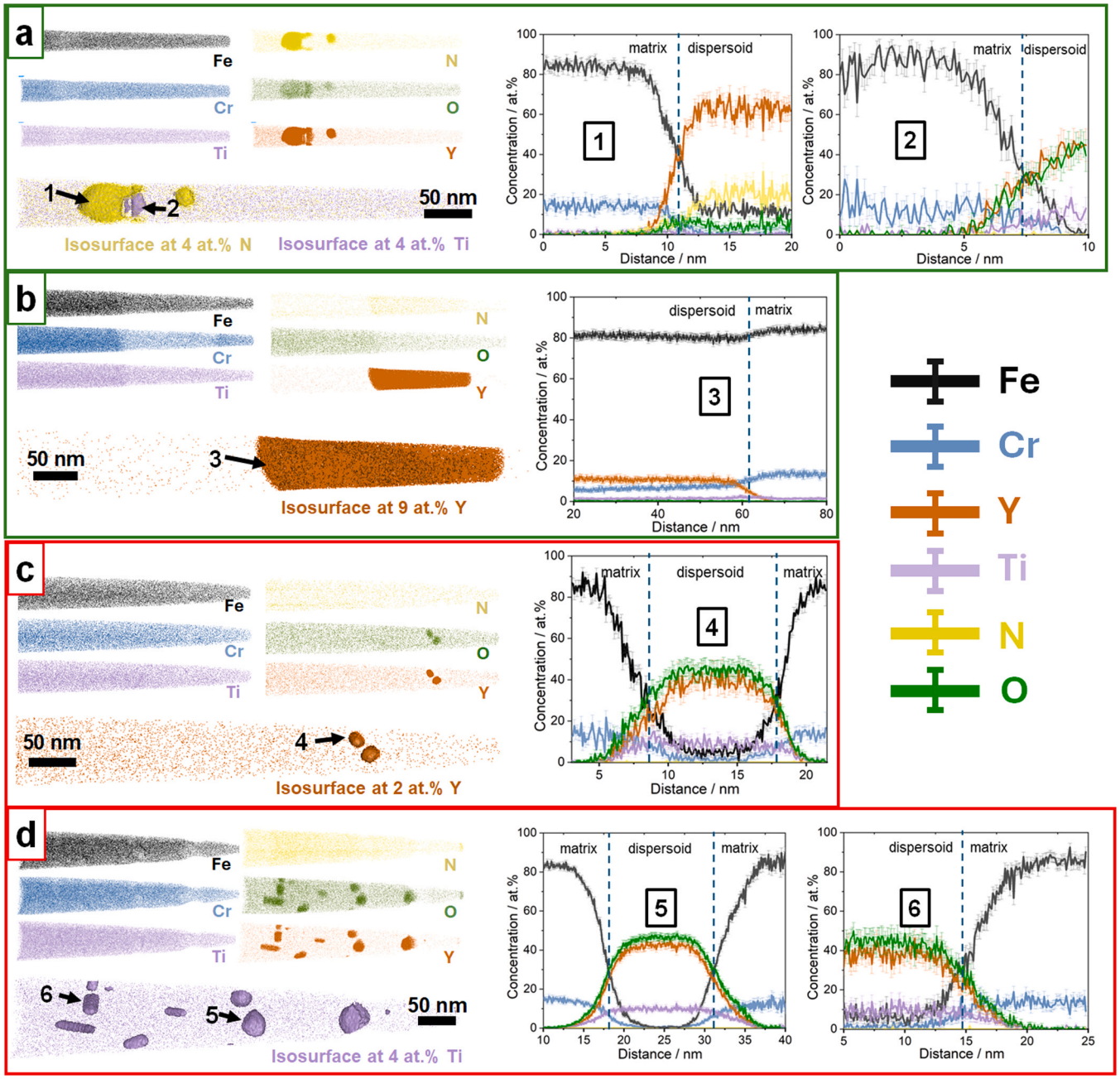

Fig. 3. Reconstructions of APT datasets including elemental distribution maps, isosurface constructions and one-dimensional concentration profiles for dispersoids for: a,b) AA powder and c,d) HT powder.

phases and are specifically no nanoclusters or segregation. Accordingly, the regions contained within the isosurfaces will hereafter be designated simply as dispersoids.

For the first tip (Fig. 3a), the resulting isosurfaces reveal two distinct types of dispersoids which are labeled as Dispersoids 1 and 2 in Fig. 3a. Dispersoid 1 corresponds to the region identified from the N isosurface. It should be noted that the Y isosurface encompassed both types of dispersoids, indicating that Y is enriched in both phases. The chemical compositions of each dispersoid as well as of the matrix are listed in Table 5. Dispersoid 1 is enriched primarily in Y (~62 at%), N (~20 at %), Fe (11 at%) with some traces of O and Ti. This composition indicates the presence of a complex Y-oxynitride. Dispersoid 2, however, is significantly different from Dispersoid 1. The 1D concentration profile of Dispersoid 2 reveals a Y–Ti–O oxide with Y (~42 at%), O (~45 at%) and Ti (~10 at%). It is completely depleted in Fe, Cr and N. For the second tip (Fig. 3b), Dispersoid 3 is not enriched in O or N and exhibits a composition that is close to an intermetallic phase with approximately Fe (~80 at%), Cr (~6 at%), and Y (~12 at%). Notably, this composition is very similar to that of the intermetallic phase observed within the interdendritic regions of the as-cast microstructure, see Table 3.

To determine the crystal structure of the dispersoids, transmission electron microscopy (TEM) analyses were carried out on one AA powder particle with a medium dispersoid density like the one for APT. The results are shown in Figure S5 of the Supplementary Material. It can be clearly seen that the dispersoid captured in TEM is an intermetallic phase with a crystal structure of the $ThMn_{12}$ prototype (space group no. 139), exactly like the intermetallic phase observed in the as-cast microstructure (Fig. 1).

It is likewise essential to determine the composition of the dispersoids for the HT condition. This approach enables determining whether their composition differs from those seen in the AA condition. Fig. 3c–d presents the APT results obtained from two tips of the HT powder. Fe, Cr, and Ti exhibit uniform distributions, whereas O and Y display evident inhomogeneity in both tips. In contrast to the AA tips, however, no inhomogeneity associated with N is observed in the HT tips. Two different isosurfaces were utilized here, i.e. 2 at% Y (Figs. 3c) and 4 at% Ti (Fig. 3d). 1D concentration profiles were extracted along cylindrical ROIs for the selected dispersoids, labeled Dispersoids 4 (Fig. 3c) as well as 5 and 6 (Fig. 3d), consistent with the methodology used in Fig. 3a–b. All three dispersoids exhibit nearly identical compositions, consisting of approximately Y (~42 at%), O (~45 at%), and Ti (~10 at%). This composition closely resembles that of the oxide dispersoids identified in the AA condition. It must be noted that the concentrations of unmarked dispersoids were also studied, and their compositions are consistent with those of the marked ones. Considering the composition of the oxide dispersoids in both the AA and HT conditions are very similar, these dispersoids are henceforth named $Y_{42}Ti_{10}O_{45}$.

Although only two tips per powder condition are shown here, multiple APT runs were carried out to capture dispersoids within the tips. Of the seven successful AA tips, only two contained dispersoids, whereas both successful HT tips revealed dispersoids. The absence of dispersoids in the remaining AA tips can be explained by the distances reported in Table 4. For a medium dispersoid number density (where the lift-outs were made), the mean distance was (0.9 ± 0.4) μm, which, relative to the tip size of a few hundred nm, indicates that the analyzed volume simply did not intersect a dispersoid.

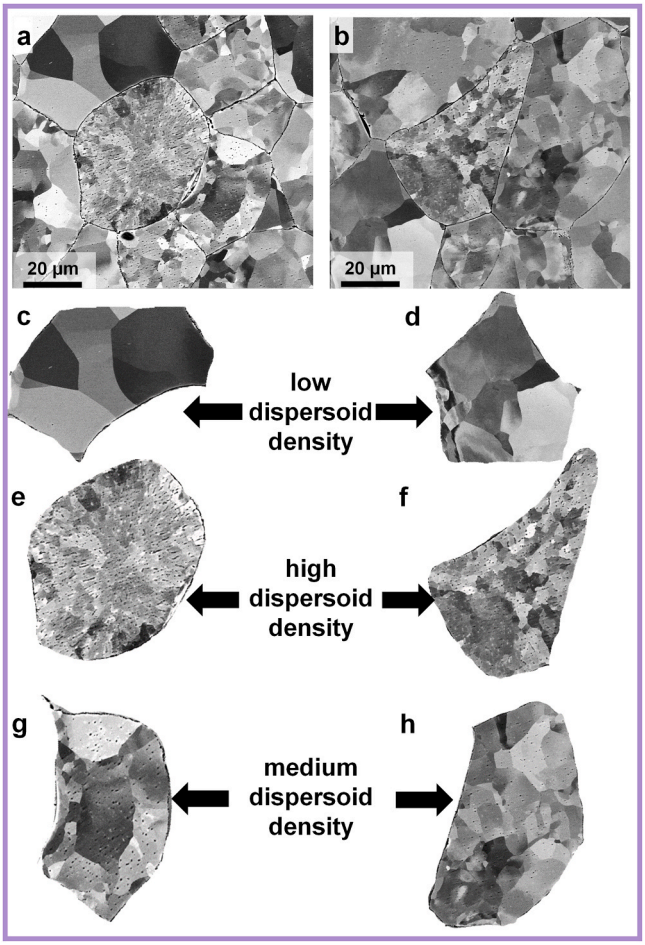

Fig. 4. SEM-BSE micrographs obtained in the FAST sample: (a,b) overviews, and enlarged former powder particles containing (c,d) low, (e,f) high and (g,h) medium dispersoid number density.

Supplementary Material Table S1 presents the Y distribution in all successfully reconstructed tips from both the AA and HT conditions, along with the corresponding bulk elemental compositions obtained across all analyzed tips. It is noteworthy that in tips lacking dispersoids, the Y content is nearly zero. This clearly indicates that the available Y in all powder particles is almost entirely consumed in the formation of dispersoids, leaving negligible Y dissolved in the matrix.

Table 5
Chemical composition of dispersoids (at%) marked 1–6 in Fig. 3 and their surrounding matrix.

Tips	Dispersoid /Matrix	Average composition / at%					
		Fe	Cr	Ti	Y	O	N
Tip 1	Disp. 1	11.6 ± 1.1	0.9 ± 0.1	0.05 ± 0.02	62.7 ± 3.4	3.3 ± 0.9	20.4 ± 2.1
(Fig. 3a)	Disp. 2	1.5 ± 0.9	0.02 ± 0.01	9.7 ± 1.2	41.9 ± 2.3	45.2 ± 1.9	0.04 ± 0.02
	Matrix	**83.5 ± 3.2**	**14.9 ± 2.1**	**1.3 ± 0.5**	**0.09 ± 0.01**	**0.2 ± 0.1**	**0**
Tip 2	Disp.3	80.2 ± 3.3	6.34 ± 1.2	1.4 ± 0.5	11.6 ± 2.1	0.1 ± 0.1	0
(Fig. 3b)	**Matrix**	**84.1 ± 2.8**	**13.3 ± 1.9**	**1.3 ± 0.42**	**0.010 ± 0.001**	**0.2 ± 0.1**	**0**
Tip 3	Disp.4	3.8 ± 0.8	0.8 ± 0.1	9.2 ± 1.3	41.5 ± 2.5	44.3 ± 4.1	0.01 ± 0.01
(Fig. 3c)	**Matrix**	**84.8 ± 2.4**	**14.7 ± 1.6**	**0.4 ± 0.19**	**0.050 ± 0.002**	**0.2 ± 0.1**	**0**
Tip 4	Disp.5	0.5 ± 0.1	0.8 ± 0.2	9.6 ± 1.7	41.9 ± 3.1	46.9 ± 2.1	0.02 ± 0.01
(Fig. 3d)	Disp.6	2.2 ± 1.2	0.7 ± 0.1	10.4 ± 1.6	41.4 ± 3.2	44.9 ± 3.1	0.02 ± 0.01
	Matrix	**84.9 ± 2.1**	**14.1 ± 1.3**	**0.4 ± 0.1**	**0.010 ± 0.01**	**0.3 ± 0.1**	**0**

3.4. Consolidated material

To produce bulk samples, AA powder was consolidated using FAST to obtain a pellet with a diameter of 20 mm and a height of 10 mm. Initial consolidation was carried out at 1100 °C to for consistency with the HT condition. However, pellets processed at this temperature were incompletely sintered, exhibiting large cavities and significant porosity of about (3.2 ± 0.9) vol% predominantly along the sinter joints. Consequently, the processing temperature was slightly increased to 1130 °C. At this higher temperature, a dense and well-consolidated sample was achieved with a porosity of (0.7 ± 0.2) vol%. Therefore, all subsequent discussions of the FAST samples refer to specimens sintered at 1130 °C. SEM-BSE micrographs of two similar regions in the FAST sample consolidated at 1130 °C are shown in Fig. 4a–b. The chemical composition of the FAST sample is provided in Table 6.

The individual powder particles making up the FAST sample remain distinguishable in SEM-BSE due to the detectable sinter boundaries. Like in the AA powder, the spatial distribution of the dispersoids (dark spots) is notably non-uniform. Classification of different regions based on dispersoid number density measured in micrographs of a uniform reference area (130 μm^2), is feasible owing to the pronounced spatial heterogeneity of dispersoid distribution. Regions within the FAST sample can again be categorized into regions of low, medium, and high dispersoid density as used in Table 3. For enhanced visualization, two representative regions from each category were selected and their microstructures magnified.

To establish a correlation between the observed dispersoid number density and the local Y concentration within the respective particles, SEM-EDS analyses were performed in regions corresponding to high, medium, and low dispersoid number density. The resulting data are summarized in Table 7. From these measurements, a clear relationship emerges. Powder particles exhibiting a high dispersoid density also possess an elevated Y content (2.46 wt%). In contrast, Y was not detected in particles with low dispersoid density (considering the Y detection limit of SEM-EDS), while powder particles with medium dispersoid densities display intermediate Y concentrations, as expected.

3.5. Microhardness testing

Given that ODS alloys are primarily designed for structural applications, it is crucial to evaluate their mechanical properties. Due to the heterogeneous distribution of dispersoids in the present alloy, Vickers microhardness tests were performed on the consolidated FAST sample. The FAST sample was selected instead of individual powder particles because hardness measurements on powder embedded in resin could yield unreliable results, as the resin's low stiffness may influence the readings. In contrast, the compacted FAST sample provides a stable surface, enabling accurate and reproducible microhardness evaluation. An indentation load of 0.49 N (HV0.05) was selected to ensure that the indents remained entirely within individual powder particle. Twenty indents were made in each of the low-, medium-, and high-density regions. The hardness values along with the average grain size of the matrix and the corresponding indent are compiled in Table 8. An increase in dispersoid number density results in evident grain refinement and a corresponding enhancement in hardness.

Table 6
Chemical composition of FAST sample obtained by ICP-OES and CGHE. The nominal composition has also been added for comparison.

Specimen Condition	Average composition / wt%					
	Fe	Cr	Ti	Y	O	N
Desired	85.1	14	0.4	0.5	-	-
FAST	83.2 ± 0.3	13.2 ± 0.1	0.42 ± 0.01	0.29 ± 0.01	0.09 ± 0.01	0.003 ± 0.001

Table 7
Composition of individual powder particles in the FAST specimen using SEM-EDS.

Dispersoid number density	Average Composition / wt%			
	Fe	Cr	Ti	Y
Low	85.4 ± 0.3	14.29 ± 0.1	0.3 ± 0.1	0
Medium	85.2 ± 0.3	13.92 ± 0.1	0.5 ± 0.1	0.4 ± 0.1
High	83.8 ± 0.3	13.04 ± 0.1	0.7 ± 0.1	2.5 ± 0.1

4. Discussion

Y-enriched intermetallic phases (enrichment with respect to the surrounding matrix) were observed in the interdendritic regions of cast microstructures as well as in the form of dispersoids in the AA powder. In both cases, a $ThMn_{12}$ prototype phase was identified via SEM-EBSD corresponding to the as-cast samples (Fig. 1c) and TEM corresponding to AA powder (Figure S5 of the Supplementary Material). This $ThMn_{12}$ prototype phase has been reported for the Fe-Ti-Y and Fe-Cr-Y ternary alloy systems as the τ phase with a composition of $Fe_{12-x}Ti_xY$ and $Fe_{12-x}Cr_xY$, respectively. The most common phase compositions reported are $Fe_{10.8}Ti_{1.2}Y$ [42], $Fe_{11}TiY$ [43], $Fe_{10}Cr_2Y$ [44] and $Fe_{10.5}Cr_{1.5}Y$ [45]. This indicates a wide stability range of $ThMn_{12}$ prototype phases. Although the composition of the intermetallic phase reported in Table 2 does not exactly match the ideal $Fe_{10}Cr_2Y$ stoichiometry, it is nonetheless close. The minor deviations observed may be attributed to experimental uncertainties like the difference between the large probe size and small phase size (SEM-EDS/STEM-EDS) and low detection efficiencies (APT).

To examine how the elemental concentration of O and Y change throughout the different processing stages (arc melting, as-atomized, heat-treated, and FAST), the corresponding concentrations of Y and O (in wt%) are presented for every processing stage in Fig. 5. The concentrations of Fe, Cr and Ti do not change significantly across the entire processing route (Tables 3–5). Therefore, only the elements mainly relevant for the dispersoid formation (Y and O) are plotted in Fig. 5.

The decrease in Y content from 0.46 wt% after arc melting to 0.29 wt % after atomization is unlikely to result from evaporation. If evaporation was occurring, a comparable loss during arc melting and drop casting needs to be obtained, yet the arc-melted and drop cast samples retain an average Y content close of 0.47 wt% (Table 2). Given that the melting points of Fe (1538 °C), Cr (1860 °C), Ti (1670 °C) and Y (1526 °C) are also quite similar to each other [35], selective evaporation of Y is unlikely. Instead, the loss in Y is most likely caused by the inhomogeneous distribution of Y between atomized particles and left-over material remaining on the platform of the ATOLab + device (material that was not atomized and cooled down slowly). This is verified by data in Figure S4 and Table S2 in the Supplementary Material. The microstructure of the left-over materials closely resembles those observed in the drop cast rods (Fig. 1). However, the overall Y concentration in the left-over material of (2.3 ± 1.7) wt% is considerably higher than the nominal composition of 0.5 wt%. Thus, the reduction of the Y concentration from 0.46 wt% to 0.29 wt% can be attributed to the loss of Y to the left-over material, not being atomized in the process. Approximately (10 ± 5)% of each atomized rod remained as unatomized left-over material. Considering the measured Y concentrations of 0.29 wt% in the atomized powder and 2.3 wt% in the left-over material, the weighted average Y content across both fractions amounts to approximately 0.49 wt%, which agrees well with the 0.47 wt% measured in the drop cast rods prior to atomization. This confirms that the reduction in Y content observed in the atomized powder is attributed to Y enrichment in the left-over material on the platform rather than to evaporation losses during the atomization process.

During subsequent heat treatment and FAST, the Y content remains relatively stable, suggesting that the major shift in Y concentration happens primarily at the atomization stage. The O content shows an

Table 8
Vickers micro-hardness test results and the average matrix grain size of the low-, medium- and high-density regions of the FAST sample along with a representative indent of each region.

Dispersoid number density ($100\ \mu m^{-2}$)	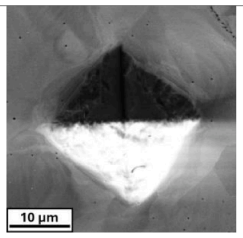 Low (< 40)	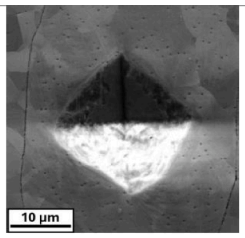 Medium (40-200)	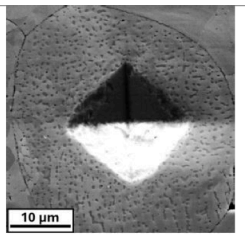 High (> 200)
Average grain size (µm)	17.4 ± 4.1	8.0 ± 2.3	2.4 ± 1.5
Hardness (HV0.05)	159 ± 7	190 ± 9	282 ± 18

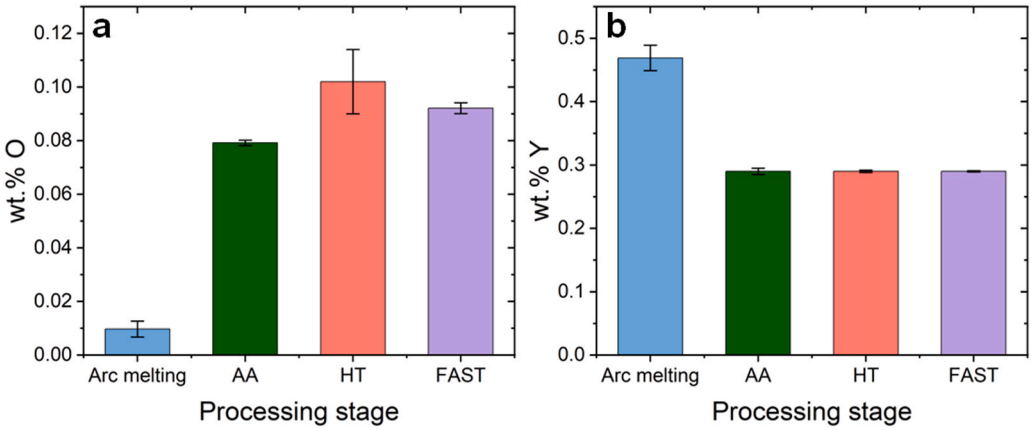

Fig. 5. Evolution of chemical concentrations through the processing route for (a) O and (b) Y.

opposite trend compared to Y during processing. O increases significantly from 0.009 wt% after arc melting to 0.079 wt% after atomization. It remains relatively stable during the heat treatment and field-assisted sintering technique steps. The O uptake during atomization has been proven to be critical for the formation of the oxide dispersoids in this step by the present work confirming the formation of oxide particles right during the atomization step.

Using the ICP-OES average Y concentration of 0.29 wt% in the atomized powder and assuming all Y is consumed to form $Y_{42}Ti_{10}O_{45}$ dispersoids, the O required for this stoichiometry would be about 0.057 wt%. The average O content in the atomized powder (0.079 wt%) exceeds the requirement for complete formation of $Y_{42}Ti_{10}O_{45}$ by approximately 40%. However, local compositional variations within individual powder particles may significantly influence the relative formation of oxide dispersoids versus intermetallic phases.

Medium-dispersoid-density powder particles (0.4 wt% Y) represent balanced conditions where the Y content closely matches the available oxidation capacity (~0.077 wt% O required), indicating predominantly oxide formation with only small amounts of intermetallic phase formed. Low dispersoid density particles, which possess even lower Y content, would primarily form oxide dispersoids. In contrast, high dispersoid density powder particles (2.5 wt% Y) encounter local O deficiency, as the stoichiometric O requirement (~0.48 wt%) greatly exceeds the available O content (0.079 wt%). Since the matrix is devoid of Y, all available Y must participate in dispersoid formation. Therefore, only ~0.41 wt% Y would be incorporated into $Y_{42}Ti_{10}O_{45}$ dispersoids, while the remaining ~2.09 wt% Y would form the Fe–Cr–Y intermetallic, resulting in markedly elevated intermetallic content in high dispersoid density powders.

This estimation assumes that the O concentration in each powder particle equals the average O concentration. In reality, this assumption may not hold true, and the precise oxide-to-intermetallic ratios will vary substantially across individual particles depending on their specific local Y and O concentrations.

The Y–Ti–O-type nanocluster dispersoids generally reported in the literature are Y_2TiO_5 and $Y_2Ti_2O_7$ [5,6]. Besides these, there are also certain other types of oxide nanoclusters with compositions around $Ti_{35}Y_{17}O_{40}$ as reported by Schneibel et al. [12]. The $Y_{42}Ti_{10}O_{45}$ oxide dispersoids (not nanoclusters, Fig. 3a-b) obtained in the AA and HT condition are, however, of a seemingly different composition, especially with respect to the Y-to-Ti ratio. While APT artifacts such as trajectory aberrations at the matrix-dispersoid interface and preferential evaporation of O cannot be entirely excluded, the LEAP 4000 XR's reflectron design minimizes such effects through improved mass resolution and spatial accuracy. Trajectory aberrations in APT are most significant for particles smaller than ~5 nm, where the interfacial distortion zone (~1–2 nm) constitutes a substantial fraction of the total particle volume. This size-dependence was directly quantified by Hatzoglou et al. [46] where the measured O content increased systematically with particle size: from 4.9 at% for particles of 0–1 nm, to 7.1 at% for 2–3 nm, to 13.4 at% for 4–5 nm, and to 22.3 at% for particles of 9–10 nm, compared to the expectation of 62.5 at% for stoichiometry of Y_2TiO_5.

For particles above 10 nm, the O content is expected to approach stoichiometric values, making the ~100 nm dispersoids in this study effectively immune to size-dependent compositional artifacts.

Besides the size effect, neutral evaporation of O atoms may lead to a deficit in the measured O quantity. In studies where the oxide phase was independently confirmed by synchrotron XRD or HRTEM, APT-measured O contents were consistently sub-stoichiometric. For particles structurally identified as $Y_2Ti_2O_7$ or Y_2TiO_5, London et al. [47,48] reported O deficit of ~16 at%. Most critically, Hatzoglou et al. [46] measured a bulk $Y_2Ti_2O_7$ crystal of known stoichiometry in APT obtaining (56.9 ± 0.3) at% O compared to 63.8 at%. A deficit of 6.9 at% attributable solely to neutral evaporation. Consequently, the measured O content in this study may be subject to similar underestimation.

While neutral evaporation systematically underestimates the absolute O content, the detection of heavier substitutional elements such as Y and Ti remains largely unaffected; the Y:Ti ratio is therefore expected to be a more reliable compositional indicator. The Y:Ti ratio of 4.2 measured in the present study substantially exceeds any value reported in the APT literature for Y–Ti–O dispersoids in ODS alloys, where ratios of 0.1–2.0 are typically observed for $Y_2Ti_2O_7$ and Y_2TiO_5 phases. Even when accounting for the slight inflation of Y or Ti fractions arising from the O deficit, a Y:Ti ratio of 4.2 cannot be reconciled with either $Y_2Ti_2O_7$ (Y:Ti = 1.0) or Y_2TiO_5 (Y:Ti = 2.0) by measurement artifact alone, indicating that the elevated ratio reflects a genuine compositional characteristic of the dispersoids in the present alloy. This new dispersoid type might be a new stable or metastable oxide that forms under the non-equilibrium conditions of the UA process. The $Y_{42}Ti_{10}O_{45}$ composition has not been reported in established Y–Ti–O ternary [49] or Y_2O_3-TiO_2 binary phase diagram [50,51], which indicates a metastable oxide that only forms during the non-equilibrium atomization process. However, whether this phase is thermodynamically stable or metastable cannot be determined from the present experimental data alone and would require dedicated thermodynamic assessment which lies beyond the scope of this study. The presence of $Y_{42}Ti_{10}O_{45}$ dispersoids in the AA and HT condition, together with the complete depletion of Y in the matrix under these conditions (as shown in Fig. 3 and Supplementary Material Table S1), suggests that nearly all dispersoids are formed during the UA process. The absence of matrix Y consequently precludes any further nucleation or growth of dispersoids during subsequent thermal treatments (HT or FAST).

It must be noted that a complex oxynitride was also observed in the APT tips of the AA condition (Fig. 3a–b). This indicates that not only oxides but also nitrides can form during UA. However, since the ratio of O:N is ~26 for the AA powders and ~17 for the HT powders (Table 4), the number density of nitrides can be expected to be at least one order of magnitude lower than that of the oxides. The number of intermetallic dispersoids compared to that of oxides is not easy to predict due to the average dispersoid distance and the typical probe volume of APT making it difficult to deliberately hit specific dispersoids.

There are in principle only two mechanisms for the dispersoids to form via nucleation and growth during the atomization process:

1. Primary solidification of the dispersoids from the liquid phase before the matrix and
2. Precipitation from the solid phase during cooling after solidification of the powder particles

To determine which of these mechanisms is likely active, we first examine the spatial distribution of the dispersoids. Precipitation of the oxides from the solid phase would be expected to proceed via heterogeneous nucleation at the grain boundaries of the solidified powder particle. However, micrographs in Fig. 2 show a uniform dispersoid distribution of dispersoids with no preference over grain boundaries. This is the first indication that the formation of the dispersoids does proceed via primary solidification from the liquid. Secondly, the observation that the mean dispersoid size remains statistically constant across powder particles irrespective of their number density (Table 3) provides additional support for liquid-phase nucleation. A solid-state, diffusion-controlled growth mechanism would be expected to produce dispersoid sizes that scale with local Y content and cooling history, whereas a growth-termination mechanism governed by matrix solidification yields a characteristic particle size, independent of local dispersoid density.

The third evidence for the formation of dispersoids via primary solidification is the order of magnitude of the dispersoid size being ~100 nm. For an oxide nucleus to grow to 100 nm, the diffusivity of Y in the matrix (either solid or liquid) must be fast enough to enable diffusion length of at least 100 nm. Whether dispersoids originate in the solid or liquid phase can be assessed by comparing the diffusion distances that Y atoms must cover under each condition to achieve a particle size of about 100 nm.

It must be noted that the cooling rate in the atomization process is extremely high. Notably, liquid droplets are immediately cooled by the flowing Ar stream (Supplementary Material Figure S2) as soon as they are detached from the melt pool due to capillary waves and suspended into the atomization chamber. While data on exact values of cooling rates are not yet reported in the literature, cooling rates from gas atomization (10^6 K/s [52]) might be a good estimate also for the ATO-Lab + device. For the following calculation, a few reasonable assumptions are made:

1. The solidus temperature of the alloy is assumed to be similar to that of Fe−14Cr, which is approximately 1535 °C (1808 K) according to the Fe-Cr phase diagram [53].
2. The diffusivity of Y in the molten alloy at 2410 °C is assumed to be comparable to that of Fe in molten Fe at the same temperature, with an estimated value of about $9 \bullet 10^{-8}$ m^2/s [54]. This assumption is made because diffusivity data for Y in molten Fe-Cr alloys are not available in the literature.
3. The diffusivity of Y in the solid alloy is approximated by the diffusivity of Y in BCC Fe at 1500 °C, which is around 10^{-15} m^2/s. This temperature is selected based on the assumption that solid-state precipitation, if it occurs, initiates immediately after solidification and continues until the temperature decreases by approximately 500 K [55].

Taking these parameters, a diffusion length scale for the two mechanisms mentioned above can be calculated. For both cases, growth taking place within a temperature drop of 500 K is considered. This assumption along with the assumption of the cooling rate, yields a growth time of $5 \bullet 10^{-4}$ s. The diffusion distance for precipitate growth can be calculated by the equation $x \approx 2\sqrt{D\,t}$, where D is the diffusion coefficient and t refers to the time. In the solid state, the diffusion distance is approximately 1.4 nm. This reflects the extremely limited atomic mobility within solids over the available diffusion time. Given such a short diffusion distance, the growth of dispersoids to sizes on the order of 100 nm is extremely unlikely under these conditions. Even if the cooling rate were two orders of magnitude lower (10^4 K/s), the estimated diffusion length (~14 nm) remains well below the observed dispersoid size (~100 nm). Thus, solid-state growth can be excluded as the dominant mechanism over a wide range of plausible cooling rates. In contrast, the calculated diffusion distance in the liquid phase extends into the micrometer range, approximately 13 μm, indicative of the significantly enhanced atomic mobility and mass transport. This substantial difference in diffusion lengths clearly demonstrates that nucleation and growth of dispersoids to larger sizes, such as 100 nm, can be readily achieved in the liquid phase due to its higher diffusivity and more favorable kinetic conditions.

Based on the preceding arguments and considering that the melting point of the $Y_{42}Ti_{10}O_{45}$ oxide is expected to be comparable to that of Y_2O_3, being approximately 2400 °C [57], it is highly probable that the

oxide dispersoids will solidify prior to the solidification of the surrounding matrix. Given that the solidus temperatures of oxides and nitrides are expected to be significantly higher than those of the intermetallic dispersoids, and considering that these phases form from the liquid state, it is reasonable to infer that oxides and oxynitrides form first, consuming the available O. Subsequently, the remaining Y contributes to the formation of intermetallic dispersoids.

While it is confirmed that the formation of oxide dispersoids through Y internal oxidation is thermodynamically feasible, the reasons for the uneven particle size and distribution must be explored. During the UA process, the alloy on top of the sonotrode is maintained in a molten state for approximately 3–5 min while the atomization process is running. Although the material is continuously heated with a moving electric arc, a local temperature drop is unavoidable. This might have caused a relative segregation of the lighter element, under the influence of convection diffusion and gravity, hence, leading to a variation in Y concentration between powder atomized from the top and bottom regions of a single melt pool. This is also the reason why the left-over material showed a much larger Y concentration (see Supplementary Material Table S2).

The hardness data presented in Table 8 reveal a distinct correlation between dispersoid density and microhardness. Regions characterized by a higher dispersoid density exhibit increased microhardness values. This enhancement can be attributed to the combined effects of a greater dispersoid density and a finer grain structure within these areas, acting synergistically to impede dislocation motion [56,57]. In contrast, regions with lower dispersoid density display reduced microhardness due to decreased hinderance to dislocation motion owing to the lesser density of dispersoids and the presence of coarser grains [58,59]. To quantitatively deconvolute the respective contributions of dispersoid and grain boundary strengthening, the Orowan-Ashby equation and the Hall-Petch relation are applied to the microstructural parameters of the high-dispersoid-density regions, where the strengthening effect is most pronounced.

The Orowan-Ashby equation quantifies the yield strength increment $\Delta\sigma_{or}$ arising when dislocations bow around and bypass incoherent particles rather than shearing through them as follows [39,60,61]:

$$\Delta\sigma_{or} = \frac{0.4 M G b}{\lambda \pi \sqrt{1-\nu}} \left(\ln \frac{2r}{b}\right) \tag{2}$$

where $\Delta\sigma_{or}$ is the increase in yield strength due to Orowan looping, M is the Taylor factor, G is the shear modulus of the matrix, b is the Burgers vector, ν is Poisson's ratio, r is the mean radius of the dispersoids, and λ is the inter-dispersoid spacing (between dispersoid interfaces, edge-to-edge) given by $\lambda = L - 2r$, where L is defined as in Equ. (1).

The contribution of the grain boundaries to strengthening is given by the Hall-Petch relation [62,63]:

$$\Delta\sigma_{HP} = \frac{k_y}{\sqrt{d}} \tag{3}$$

where $\Delta\sigma_{HP}$ is the Hall-Petch strengthening, k_y is the Hall-Petch coefficient and d is the average grain size. The following material constants are used: $M = 3.06$ [64] for a randomly textured BCC polycrystal, $G =$ 83GPa as the shear modulus for BCC Fe-Cr [65], $b = 0.248$nm as the Burgers vector of ½⟨111⟩ dislocations in BCC Fe-Cr [66], calculated from the lattice parameter of pure Fe and consistent with values used throughout the ODS literature, and $\nu = 0.30$ as the Poisson's ratio for BCC Fe-Cr alloys [67]. The microstructural parameters r and L are taken directly from Table 3, and d is taken from Table 8. A Hall-Petch coefficient of $k_y = 560\ MPa{\cdot}\mu m^{0.5}$ representative of ferritic Fe-Cr steels is adopted following Takaki et al. [68]. Taking these values, $\Delta\sigma_{or}$ is 164 MPa while $\Delta\sigma_{HP}$ is 361 MPa, which suggests that grain boundary strengthening is the dominant strengthening mechanism, contributing approximately 69% of the total strengthening increment, with Orowan strengthening accounting for the remaining 31%. It should be noted that this analysis considers only the Orowan and Hall-Petch contributions and does not account for additional strengthening mechanisms that may be active in the present alloy, including solid solution strengthening, residual dislocation strengthening from FAST consolidation, and the intrinsic Peierls-Nabarro lattice friction stress. Nevertheless, despite its simplicity, this two-term analysis provides a meaningful estimate of the major contributions of dispersoid and grain boundary strengthening, which are expected to be the dominant mechanisms in this alloy system.

Given that the present work introduces a novel synthesis route, it is essential to contextualize the obtained hardness values by comparing them with those reported for ferritic ODS alloys in the literature. In terms of alloy composition, atomization and consolidation conditions, as well as post-processing treatments, a systematic comparison of hardness values remains challenging due to the substantial variations reported over several decades of research on Fe-based ODS systems. Nevertheless, meaningful comparisons can still be made with studies that employ similar consolidation routes to the present work without any subsequent post-processing, hence differing only in the atomization method.

Franke et al. [69] reported Vickers hardness values ranging from 238 to 322 HV10 for Fe−9Cr ODS steels, with hardness increasing with milling duration. Similarly, Boulnat et al. [70] reported values between 250 and 330 HV10 for Fe−14Cr-1W−0.3Y_2O_3, with a peak hardness of (332 ± 6) HV10 achieved in the most densified compacts. Under a lower load, the hardness further increased to (377 ± 67) HV0.05. In general, hardness values decrease with increasing indentation load, a trend frequently reported for ferritic alloys within the 200–400 HV range [71]. This behavior is also evident in Ref. [70], where reducing the load from HV10 to HV0.05 resulted in higher hardness values. Hence, the hardness values obtained in the present study are expected to be about 30–50 HV lower than the MA studies reported in the literature, if the load could be maintained equivalent across all studies.

The strengthening effect of dispersoids in the present study is, however, evident when comparing the hardness of regions with high and low dispersoid densities. The high-density regions exhibit a hardness of (282 ± 18) HV0.05, whereas the low-density regions show only (159 ± 7) HV0.05. This relative increase of 80% is comparable to that observed in Eurofer97, where the presence of dispersoids raises the hardness from ~235 HV0.1 (no dispersoids) to ~365 HV0.1 [72]. While studies commonly report ultrafine-grained microstructures (10–50 nm) with dispersoid sizes in the range of 5–50 nm in samples produced via the MA route [5,6,73], the current UA-processed alloy exhibits a larger, average grain size of approximately 2 μm (Table 8) and coarser dispersoids with a mean radius of (101 ± 70) nm (Table 3).

While volume fractions of dispersoids are not always explicitly reported in the cited studies on MA Fe-Cr ODS alloys, the data available consistently indicate typical dispersoids volume fractions of around 0.2–0.3 vol% for nanosized Y_2O_3 or Y–Ti–O nanoclusters quantified via TEM and APT [74–76]. In contrast, high-density regions of the UA powders exhibit a markedly higher dispersoid volume fraction of up to (12.5 ± 2.4) vol% (Table 3). Using these data, the dominant strengthening mechanism can further be understood through the analysis of the Zener grain size d_Z and its critical value d_Z^* according to Hazzledine [77] and Schneibel and Heilmaier [78]. The Zener grain size d_Z is reached when the driving force for grain boundary motion due to curvature is balanced by the pinning force caused by the dispersoids:

$$d_Z = C_Z \frac{2r}{f} \tag{4}$$

with C_Z as a parameter[1] between 1/6 and 4/3. The Zener grain size represents an upper limit of grain size for which coarsening occurs if no other driving force is active than grain boundary curvature. The critical Zener grain size d_Z^* indicates a critical size beyond which strengthening

[1] See Ref. [78] for a detailed discussion of C_Z.

shifts from being controlled by dispersoids (Orowan) to grain boundaries (Hall-Petch):

$$d_Z^* = \frac{M^2}{6\pi f}\left(\frac{G\,b}{k_y}\right)^2 \quad (5)$$

Using the same values for the variables used to solve Equs. (2) and (3), Equ. (5) yields a $d_Z^* \approx 5.4$nm for the high-dispersoid-density regions of the UA samples ($f = 0.125$). Given the observed grain size of $d \approx 2.4$μm and other microstructure data for this case (Tables 3 and 8), the condition $d \gg d_Z > d_Z^*$ is satisfied, indicating that the microstructure operates within the grain-boundary-strengthening-dominated regime. This agrees with the strengthening estimates, where grain boundary strengthening was shown to contribute ~69% of the total strength. For MA-processed ODS alloys, the much lower $f = 0.0025$ yields a $d_Z^* \approx 268$nm. With typically ultrafine grain sizes of $d < 50$ nm, these alloys barely satisfy $d > d_Z \approx d_Z^*$, indicating that Hall-Petch does not clearly dominate over Orowan strengthening for the MA route alloys.

A similar correlation between dispersoid size, volume fraction, and strengthening was also reported by Luptáková et al. [79] who found that 5 vol% of coarser oxides of sizes greater than 20 nm provides mechanical reinforcement comparable to that in traditional dispersions containing less than 1 vol% of ultrafine oxides in the size range of 2–5 nm.

Although the hardness of the high-density region is comparable to ferritic ODS alloys produced via MA followed by sintering, the inhomogeneity of the dispersoid distribution needs to be tackled. The alloy was produced via two routes (elemental Y and Fe_2Y master alloy) with four rods per route, as previously described. As both routes showed comparable inhomogeneity in Y and dispersoid distribution, this behavior is attributed to the UA process itself rather than batch-to-batch variations. This reproducibility confirms that the identified microstructural trends and phase evolution mechanisms are representative and reliable. Potential strategies to improve dispersoid homogeneity include fine-tuning of atomization parameters, adoption of wire rather than rod feeding to reduce melt pool size and limit Y segregation, and the introduction of deformation-assisted consolidation routes [80,81]. As the present study primarily aims to establish the thermodynamic and kinetic feasibility of the proposed method for producing ODS powders, a detailed investigation of process parameter optimization and post-processing lies beyond its current scope and will be addressed in future work.

5. Conclusions

The Fe−14Cr−0.5Ti−0.5Y ferritic ODS alloy is manufactured via powder metallurgy route using a novel ultrasonic atomization (UA) technique with elemental Y rather than Y_2O_3. The formation mechanism of dispersoids and their distribution in the powders are investigated. Based on experimental observations, the following conclusions can be made.

- Using the UA technique, Y–Ti–O *nanoclusters* do not form. However, the technique successfully produces $Y_{42}Ti_{10}O_{45}$ dispersoids in the size range of 20–100 nm in the atomized powder. In addition to the oxides, oxynitrides and intermetallic dispersoids are also formed. This positively answers research question number 1.
- The formation of dispersoids occurs through homogeneous nucleation and growth directly from the liquid phase. This is supported by evidence based on the spatial distribution of the dispersoids as well as the diffusion distances of Y to grow to 100 nm or larger. This clarifies research question number 2.
- The dispersoids remain chemically stable when subjected to thermal exposure during heat treatment of powder or during sintering via FAST. Although formation of dispersoids is achieved during the UA process, their number, size, and spatial distribution vary significantly from one powder particle to another and strongly depend on the Y content present in each powder particle at the time of atomization. The inhomogeneity in the dispersoid density across different powder particles is attributed to the non-uniform Y concentration in the melt pool in the UA device. Research question number 3 must be answered negatively.
- Despite the substantially coarser grain and dispersoid sizes observed in the UA powder and FAST material compared to mechanically alloyed counterparts, the resulting hardness values are comparable, albeit slightly lower by approximately 30–50 HV. The pronounced hardness increase of about 80% between regions with low and high dispersoid densities underscores the major impact of dispersoid density to strengthening. Overall, these findings demonstrate that the present synthesis method offers a promising alternative to conventional mechanical alloying for producing dispersion-strengthened ferritic alloys. This answers research question number 4.

CRediT authorship contribution statement

Daniel Schliephake: Writing – review & editing, Investigation, Formal analysis. **Christoph Somsen:** Writing – review & editing, Investigation, Formal analysis. **Sascha Seils:** Writing – review & editing, Investigation, Formal analysis, Conceptualization. **Marcel Muench:** Writing – review & editing, Investigation, Formal analysis. **Liu Yang:** Writing – review & editing, Investigation, Formal analysis. **Sandipan Sen:** Writing – review & editing, Writing – original draft, Visualization, Project administration, Investigation, Formal analysis, Data curation. **Shubhashis Dixit:** Writing – review & editing, Writing – original draft, Investigation, Formal analysis, Data curation. **Alexander Kauffmann:** Writing – review & editing, Writing – original draft, Visualization, Supervision, Funding acquisition, Formal analysis, Data curation, Conceptualization. **Martin Heilmaier:** Writing – review & editing, Supervision, Resources, Funding acquisition, Conceptualization.

Declaration of Competing Interest

The authors declare the following financial interests/personal relationships which may be considered as potential competing interests: AK and MH reports financial support was provided by German Research Foundation. LY reports financial support was provided by China Scholarship Council. All report equipment and supplies was provided by Karlsruhe Institute of Technology (KNMFi and IAM-AWP). If there are other authors, they declare that they have no known competing financial interests or personal relationships that could have appeared to influence the work reported in this paper.

Acknowledgements

We gratefully acknowledge financial support from the Deutsche Forschungsgemeinschaft (DFG), project no. 462420328. LY is financially supported by China Scholarship Council (CSC) with No. 202207000023. This work was partly carried out with the support of the Karlsruhe Nano Micro Facility (KNMFi, www.knmf.kit.edu), a Helmholtz Research Infrastructure at Karlsruhe Institute of Technology (KIT, www.kit.edu). We acknowledge the chemical analysis by HCGE at the Institute for Applied Materials (IAM-AWP) by Dr. Bergfeldt, Karlsruhe Institute of Technology (KIT).

Appendix A. Supporting information

Supplementary data associated with this article can be found in the online version at doi:10.1016/j.jallcom.2026.188928.

Data Availability

The data presented in this study are available in KITopen at https://

doi.org/10.5281/zenodo.17508782 under CC BY-SA 4.0 license. Further information is available upon request with alexander.kauffmann@rub.de.

References

[1] M. Praud, F. Mompiou, J. Malaplate, D. Caillard, J. Garnier, A. Steckmeyer, B. Fournier, Study of the deformation mechanisms in a Fe–14% Cr ODS alloy, J. Nucl. Mater. 428 (2012) 90–97, https://doi.org/10.1016/j.jnucmat.2011.10.046.

[2] C. Zakine, C. Prioul, D. François, Creep behaviour of ODS steels, Mater. Sci. Eng. A 219 (1996) 102–108, https://doi.org/10.1016/S0921-5093(96)10415-9.

[3] D.K. Mukhopadhyay, F.H. Froes, D.S. Gelles, Development of oxide dispersion strengthened ferritic steels for fusion, J. Nucl. Mater. 258263 (1998) 1209–1215, https://doi.org/10.1016/S0022-3115(98)00188-3.

[4] M.B. Toloczko, D.S. Gelles, F.A. Garner, R.J. Kurtz, K. Abe, Irradiation creep and swelling from 400 to 600 °C of the oxide dispersion strengthened ferritic alloy MA957, J. Nucl. Mater. 329333 (2004) 352–355, https://doi.org/10.1016/j.jnucmat.2004.04.296.

[5] S. Seils, A. Kauffmann, W. Delis, T. Boll, M. Heilmaier, Microstructure and mechanical properties of high-Mn-ODS steels, Mater. Sci. Eng. A 825 (2021) 141859, https://doi.org/10.1016/j.msea.2021.141859.

[6] S. Seils, A. Kauffmann, F. Hinrichs, D. Schliephake, T. Boll, M. Heilmaier, Temperature dependent strengthening contributions in austenitic and ferritic ODS steels, Mater. Sci. Eng. A 786 (2020) 139452, https://doi.org/10.1016/j.msea.2020.139452.

[7] D.S. Gelles, Research and development of iron-based alloys for nuclear technology, ISIJ Int. 30 (1990) 905–916, https://doi.org/10.2355/isijinternational.30.905.

[8] L.L. Hsiung, M.J. Fluss, S.J. Tumey, B.W. Choi, Y. Serruys, F. Willaime, A. Kimura, Formation mechanism and the role of nanoparticles in Fe-Cr ODS steels developed for radiation tolerance, Phys. Rev. B 82 (2010) 184103, https://doi.org/10.1103/PhysRevB.82.184103.

[9] S. Ukai, M. Harada, H. Okada, M. Inoue, S. Nomura, S. Shikakura, T. Nishida, M. Fujiwara, K. Asabe, Tube manufacturing and mechanical properties of oxide dispersion strengthened ferritic steel, J. Nucl. Mater. 204 (1993) 74–80, https://doi.org/10.1016/0022-3115(93)90201-9.

[10] J.H. Schneibel, M. Heilmaier, W. Blum, G. Hasemann, T. Shanmugasundaram, Temperature dependence of the strength of fine- and ultrafine-grained materials, Acta Mater. 59 (2011) 1300–1308, https://doi.org/10.1016/j.actamat.2010.10.062.

[11] T.M. Smith, C.A. Kantzos, N.A. Zarkevich, B.J. Harder, M. Heczko, P.R. Gradl, A. C. Thompson, M.J. Mills, T.P. Gabb, J.W. Lawson, A 3D printable alloy designed for extreme environments, Nature 617 (2023) 513–518, https://doi.org/10.1038/s41586-023-05893-0.

[12] J.H. Schneibel, C.T. Liu, M.K. Miller, M.J. Mills, P. Sarosi, M. Heilmaier, D. Sturm, Ultrafine-grained nanocluster-strengthened alloys with unusually high creep strength, Scr. Mater. 61 (2009) 793–796, https://doi.org/10.1016/j.scriptamat.2009.06.034.

[13] Y. Li, J. Shen, F. Li, H. Yang, S. Kano, Y. Matsukawa, Y. Satoh, H. Fu, H. Abe, T. Muroga, Effects of fabrication processing on the microstructure and mechanical properties of oxide dispersion strengthening steels, Mater. Sci. Eng. A 654 (2016) 203–212, https://doi.org/10.1016/j.msea.2015.12.032.

[14] K.G. Raghavendra, A. Dasgupta, N.S. Karthiselva, K. Jayasankar, S.R. Bakshi, Microstructural characterization of novel ZrO_2 dispersion-strengthened 9Cr steel by spark plasma sintering, J. Mater. Eng. Perform. 32 (2023) 9814–9824, https://doi.org/10.1007/s11665-023-08244-2.

[15] Z. Dong, Z. Ma, L. Yu, Y. Liu, Achieving high strength and ductility in ODS-W alloy by employing oxide@W core-shell nanopowder as precursor, Nat. Commun. 12 (2021) 5052, https://doi.org/10.1038/s41467-021-25283-2.

[16] H. Xu, Z. Lu, D. Wang, C. Liu, Microstructure refinement and strengthening mechanisms of a 9Cr oxide dispersion strengthened steel by zirconium addition, Nucl. Eng. Technol. 49 (2017) 178–188, https://doi.org/10.1016/j.net.2017.01.002.

[17] M. Nagini, R. Vijay, K.V. Rajulapati, A.V. Reddy, G. Sundararajan, Microstructure–mechanical property correlation in oxide dispersion strengthened 18Cr ferritic steel, Mater. Sci. Eng. A 708 (2017) 451–459, https://doi.org/10.1016/j.msea.2017.10.023.

[18] Cs Balázsi, F. Gillemot, M. Horváth, F. Wéber, K. Balázsi, F.C. Sahin, Y. Onüralp, Á. Horváth, Preparation and structural investigation of nanostructured oxide dispersed strengthened steels, J. Mater. Sci. 46 (2011) 4598–4605, https://doi.org/10.1007/s10853-011-5359-1.

[19] A. Meza, E. Macía, A. García-Junceda, L.A. Díaz, P. Chekhonin, E. Altstadt, M. Serrano, M.E. Rabanal, M. Campos, Development of new 14 Cr ODS steels by using new oxides formers and B as an inhibitor of the grain growth, Metals 10 (2020) 1344, https://doi.org/10.3390/met10101344.

[20] C. Suryanarayana, E. Ivanov, V.V. Boldyrev, The science and technology of mechanical alloying, Mater. Sci. Eng. A 304306 (2001) 151–158, https://doi.org/10.1016/S0921-5093(00)01465-9.

[21] G. Spartacus, J. Malaplate, F. De Geuser, I. Mouton, D. Sornin, M. Perez, R. Guillou, B. Arnal, E. Rouesne, A. Deschamps, Chemical and structural evolution of nano-oxides from mechanical alloying to consolidated ferritic oxide dispersion strengthened steel, Acta Mater. 233 (2022) 117992, https://doi.org/10.1016/j.actamat.2022.117992.

[22] T. Gräning, M. Rieth, J. Hoffmann, S. Seils, P.D. Edmondson, A. Möslang, Microstructural investigation of an extruded austenitic oxide dispersion strengthened steel containing a carbon-containing process control agent, J. Nucl. Mater. 516 (2019) 335–346, https://doi.org/10.1016/j.jnucmat.2019.01.048.

[23] S. Ukai, M. Harada, H. Okada, M. Inoue, S. Nomura, S. Shikakura, K. Asabe, T. Nishida, M. Fujiwara, Alloying design of oxide dispersion strengthened ferritic steel for long life FBRs core materials, J. Nucl. Mater. 204 (1993) 65–73, https://doi.org/10.1016/0022-3115(93)90200-I.

[24] C.A. Williams, E.A. Marquis, A. Cerezo, G.D.W. Smith, Nanoscale characterisation of ODS–Eurofer 97 steel: an atom-probe tomography study, J. Nucl. Mater. 400 (2010) 37–45, https://doi.org/10.1016/j.jnucmat.2010.02.007.

[25] M.J. Alinger, G.R. Odette, D.T. Hoelzer, The development and stability of Y–Ti–O nanoclusters in mechanically alloyed Fe–Cr based ferritic alloys, J. Nucl. Mater. 329333 (2004) 382–386, https://doi.org/10.1016/j.jnucmat.2004.04.042.

[26] C. Heintze, M. Hernández-Mayoral, A. Ulbricht, F. Bergner, A. Shariq, T. Weissgärber, H. Frielinghaus, Nanoscale characterization of ODS Fe–9%Cr model alloys compacted by spark plasma sintering, J. Nucl. Mater. 428 (2012) 139–146, https://doi.org/10.1016/j.jnucmat.2011.08.053.

[27] U. Martin, M. Heilmaier, Novel dispersion strengthened metals by mechanical alloying, Adv. Eng. Mater. 6 (2004) 515–520, https://doi.org/10.1002/adem.200400410.

[28] B.S. Murty, S. Ranganathan, Novel materials synthesis by mechanical alloying/milling, Int. Mater. Rev. 43 (1998) 101–141.

[29] M. Heilmaier, H. Saage, J. Eckert, Formation of ODS $L1_2$–$(Al,Cr)_3Ti$ by mechanical alloying, Mater. Sci. Eng. A 239240 (1997) 652–657, https://doi.org/10.1016/S0921-5093(97)00644-8.

[30] Y. Wu, Q. Huang, L. Zhang, Y. Jiang, G. Zhu, J. Shen, Microstructure and mechanical properties of $Y_4Zr_3O_{12}$-Added Fe–13.5Cr–2W oxide-dispersion-strengthened steels, containing high contents of C and N, prepared by mechanical alloying and two-step spark plasma sintering, Materials 16 (2023) 2433, https://doi.org/10.3390/ma16062433.

[31] Z. Oksiuta, N. Baluc, Optimization of the chemical composition and manufacturing route for ODS RAF steels for fusion reactor application, Nucl. Fusion. 49 (2009) 055003, https://doi.org/10.1088/0029-5515/49/5/055003.

[32] Y. Zhang, Y. Yan, Y. Zhai, W. Qin, H. Che, T. Wang, R. Cao, Effect of oxygen content on microstructure and tensile properties of a 22Cr-5Al ODS steel, Materials 14 (2021), https://doi.org/10.3390/ma14092241.

[33] N. Oono, S. Ukai, Precipitation of oxide particles in oxide dispersion strengthened (ODS) ferritic steels, Mater. Trans. 59 (2018) 1651–1658, https://doi.org/10.2320/matertrans.M2018110.

[34] B. Bałasz, M. Bielecki, W. Gulbiński, Słoboda, Comparison of ultrasonic and other atomization methods in metal powder production, J. Achiev. Mater. Manuf. Eng. 116 (2023) 11–24, https://doi.org/10.5604/01.3001.0016.3393.

[35] J.R. Davis, in: Metals handbook desk edition, 2nd ed., ASM international, 1998.

[36] N. García-Rodríguez, Capability of mechanical alloying and SPS technique to develop nanostructured high Cr, Al alloyed ODS steels, Mater. Sci. Technol. 30 (2014) 1676–1684, https://doi.org/10.1179/1743284714Y.0000000595.

[37] R. Gerling, R. Leitgeb, F.P. Schimansky, Porosity and argon concentration in gas atomized γ-TiAl powder and hot isostatically pressed compacts, Mater. Sci. Eng. A 252 (1998) 239–247, https://doi.org/10.1016/S0921-5093(98)00656-X.

[38] C. Cui, F. Stern, N. Ellendt, V. Uhlenwinkel, M. Steinbacher, J. Tenkamp, F. Walther, R. Fechte-Heinen, Gas atomization of duplex stainless steel powder for laser powder bed fusion, Materials 16 (2023) 435, https://doi.org/10.3390/ma16010435.

[39] B. Reppich, Chapter 7: Particle Strengthening. Materials Science and Technology, Wiley-VCH, Weinheim, 1993.

[40] S. Shah, E. Thronsen, F.D. Geuser, C. Hatzoglou, C.D. Marioara, R. Holmestad, B. Holmeda, On the use of a cluster identification method and a statistical approach for analyzing atom probe tomography data for GP zones in Al–Zn–Mg(–Cu) alloys, Microsc. Microanal. 30 (2024) 1–13, https://doi.org/10.1093/micmic/ozad133.

[41] T. Ogura, S. Hirosawa, A. Cerezo, T. Sato, Atom probe tomography of nanoscale microstructures within precipitate free zones in Al–Zn–Mg(–Ag) alloys, Acta Mater. 58 (2010) 5714–5723, https://doi.org/10.1016/j.actamat.2010.06.046.

[42] Z. Liu, Z. Jin, C. Xia, 873 K Isothermal section of phase diagram for Y-Fe-Ti ternary system, Scr. Mater. 37 (1997) 1129–1134, https://doi.org/10.1016/S1359-6462(97)00234-0.

[43] O. Moze, L. Pareti, M. Solzi, W.I.F. David, Neutron diffraction and magnetic anisotropy study of Y-Fe-Ti intermetallic compounds, Solid State Commun. 66 (1988) 465–469, https://doi.org/10.1016/0038-1098(88)90962-3.

[44] D.B. De Mooij, K.H.J. Buschow, Some novel ternary ThMn12-type compounds, J. Less Common. Met. 136 (1988) 207–215, https://doi.org/10.1016/0022-5088(88)90424-9.

[45] P. Qian, N.-X. Chen, J. Shen, Atomistic simulation for the phase stability, site preference and thermal expansion of $YFe_{12-x}T_x$ (T=Ti, V, Cr, Mn, Zr, Nb, Mo, W), Solid. State Commun. 134 (2005) 771–776, https://doi.org/10.1016/j.ssc.2005.01.048.

[46] C. Hatzoglou, B. Radiguet, P. Pareige, Experimental artefacts occurring during atom probe tomography analysis of oxide nanoparticles in metallic matrix: quantification and correction, J. Nucl. Mater. 492 (2017) 279–291, https://doi.org/10.1016/j.jnucmat.2017.05.008.

[47] A.J. London, S. Santra, S. Amirthapandian, B.K. Panigrahi, R.M. Sarguna, S. Balaji, R. Vijay, C.S. Sundar, S. Lozano-Perez, C.R.M. Grovenor, Effect of Ti and Cr on dispersion, structure and composition of oxide nano-particles in model ODS alloys, Acta Mater. 97 (2015) 223–233, https://doi.org/10.1016/j.actamat.2015.06.032.

[48] A.J. London, S. Lozano-Perez, M.P. Moody, S. Amirthapandian, B.K. Panigrahi, C. S. Sundar, C.R.M. Grovenor, Quantification of oxide particle composition in model

oxide dispersion strengthened steel alloys, Ultramicroscopy 159 (2015) 360–367, https://doi.org/10.1016/j.ultramic.2015.02.013.
[49] L. Barnard, G.R. Odette, I. Szlufarska, D. Morgan, An ab initio study of Ti–Y–O nanocluster energetics in nanostructured ferritic alloys, Acta Mater. 60 (2012) 935–947, https://doi.org/10.1016/j.actamat.2011.11.011.
[50] W. Gong, D. Li, Z. Chen, F. Zheng, Y. Liu, Y. Du, B. Huang, Phase equilibria of the system, Calphad 33 (2009) 624–627, https://doi.org/10.1016/j.calphad.2009.06.005.
[51] N. Mizutani, Y. Tajima, M. Kato, Phase relations in the system Y_2O_3 -TiO_2, –168, J. Am. Ceram. Soc. 59 (1976) 168, https://doi.org/10.1111/j.1151-2916.1976.tb09459.x.
[52] T.M. Abu-Lebdeh, G.P. León, S.A. Hamoush, R.D. Seals, V.E. Lamberti, Gas atomization of molten metal: part II. Applications, Am. J. Eng. Appl. Sci. 9 (2016) 334–349, https://doi.org/10.3844/ajeassp.2016.334.349.
[53] A. Jacob, E. Povoden-Karadeniz, E. Kozeschnik, Revised thermodynamic description of the Fe-Cr system based on an improved sublattice model of the σ phase, Calphad 60 (2018) 16–28, https://doi.org/10.1016/j.calphad.2017.10.002.
[54] A. Meyer, L. Hennig, F. Kargl, T. Unruh, Iron self diffusion in liquid pure iron and iron-carbon alloys, J. Phys. Condens. Matter 31 (2019) 395401, https://doi.org/10.1088/1361-648X/ab2855.
[55] D. Murali, B.K. Panigrahi, M.C. Valsakumar, C.S. Sundar, Diffusion of Y and Ti/Zr in bcc iron: a first principles study, J. Nucl. Mater. 219 (2011) 208–212, https://doi.org/10.1016/j.jnucmat.2011.05.018.
[56] R. Jarugula, P.S. Babu, S.G.S. Raman, G. Sundararajan, Creep deformation behavior of nano oxide dispersion strengthened Fe–18Cr ferritic steel, Materialia 12 (2020) 100788, https://doi.org/10.1016/j.mtla.2020.100788.
[57] Y. Ijiri, N. Oono, S. Ukai, S. Ohtsuka, T. Kaito, Y. Matsukawa, Oxide particle–dislocation interaction in 9Cr-ODS steel, Nucl. Mater. Energy 9 (2016) 378–382, https://doi.org/10.1016/j.nme.2016.06.014.
[58] Y. Zhang, B. Liu, R. Zhang, H. Liu, Y. Cao, J. Li, Q. Fang, Y. Liu, Development of oxide dispersion strengthened ferritic steel with enhanced strength–ductility combination through dispersion strengthening and back stress hardening, J. Mater. Res. Technol. 23 (2023) 1386–1396, https://doi.org/10.1016/j.jmrt.2023.01.060.
[59] B.W. Baker, T.R. McNelley, L.N. Brewer, Grain size and particle dispersion effects on the tensile behavior of friction stir welded MA956 oxide dispersion strengthened steel from low to elevated temperatures, Mater. Sci. Eng. A 589 (2014) 217–227, https://doi.org/10.1016/j.msea.2013.09.092.
[60] M.F. Ashby, Work hardening of dispersion-hardened crystals, Philos. Mag. 14 (1966) 1157–1178, https://doi.org/10.1080/14786436608224282.
[61] D.J. Bacon, U.F. Kocks, R.O. Scattergood, The effect of dislocation self-interaction on the orowan stress, Philos. Mag. 28 (1973) 1241–1263, https://doi.org/10.1080/14786437308227997.
[62] E.O. Hall, The deformation and ageing of mild steel: III discussion of results, Proc. Phys. Soc. Sect. B 64 (1951) 747–753, https://doi.org/10.1088/0370-1301/64/9/303.
[63] N.J. Petch, The cleavage strength of polycrystals, J. Iron Steel Inst. 174 (1953) 25–28.
[64] G.I. Taylor, Plastic strain in metals, J. Inst. Met. 62 (1938) 307–324.
[65] A. Chauhan, F. Bergner, A. Etienne, J. Aktaa, Y. De Carlan, C. Heintze, D. Litvinov, M. Hernandez-Mayoral, E. Oñorbe, B. Radiguet, A. Ulbricht, Microstructure characterization and strengthening mechanisms of oxide dispersion strengthened (ODS) Fe-9%Cr and Fe-14%Cr extruded bars, J. Nucl. Mater. 495 (2017) 6–19, https://doi.org/10.1016/j.jnucmat.2017.07.060.
[66] C. Kittel, Solid State Physics, 8th ed., Hoboken, 2005.
[67] G. Simmons, H. Wang, Single Crystal Elastic Constants and Calculated Aggregate Properties, The MIT Press, Cambridge, 1971.
[68] S. Takaki, Review on the hall-petch relation in ferritic steel, Mater. Sci. Forum 654-656 (2010) 11–16, https://doi.org/10.4028/www.scientific.net/MSF.654-656.11.
[69] P. Franke, C. Heintze, F. Bergner, T. Weißgärber, Mechanical properties of spark plasma sintered Fe-Cr compacts strengthened by nanodispersed Yttria particles, Mater. Test. 52 (2010) 133–138, https://doi.org/10.3139/120.110115.
[70] X. Boulnat, D. Fabrègue, M. Perez, S. Urvoy, D. Hamon, Y. De Carlan, Assessment of consolidation of oxide dispersion strengthened ferritic steels by spark plasma sintering: from laboratory scale to industrial products, Powder Metall. 57 (2014) 204–211, https://doi.org/10.1179/1743290114Y.0000000091.
[71] A. Xu, X. Song, M. Ye, Y. Wan, C. Zhang, Microhardness variation with indentation depth for body-centered cubic steels pertinent to grain size and ferrite content, Materials 17 (2024) 2371, https://doi.org/10.3390/ma17102371.
[72] I. Bartošová, J. Čížek, F. Lukáč, V. Slugeň, Vickers hardness and positron annihilation study of Eurofer97 and ODS Eurofer, Acta Phys. Pol. A 125 (2014) 702–705, https://doi.org/10.12693/APhysPolA.125.702.
[73] K.N. Allahar, J. Burns, B. Jaques, Y.Q. Wu, I. Charit, J. Cole, D.P. Butt, Ferritic oxide dispersion strengthened alloys by spark plasma sintering, J. Nucl. Mater. 443 (2013) 256–265, https://doi.org/10.1016/j.jnucmat.2013.07.019.
[74] G. Spartacus, J. Malaplate, F. De Geuser, I. Mouton, D. Sornin, R. Guillou, A. Deschamps, Precipitation kinetics of ferritic / martensitic oxide dispersion strengthened steels: Influence of the matrix phase transformation, Acta Mater. 280 (2024) 120328, https://doi.org/10.1016/j.actamat.2024.120328.
[75] P. Dymáček, M. Jarý, D. Bártková, N. Luptáková, Š. Gamanov, P. Bořil, V. Georgiev, J. Svoboda, High-temperature creep resistance of FeAlOY ODS ferritic alloy, Materials 17 (2024) 4984, https://doi.org/10.3390/ma17204984.
[76] N. Sallez, C. Hatzoglou, F. Delabrouille, D. Sornin, L. Chaffron, M. Blat-Yrieix, B. Radiguet, P. Pareige, P. Donnadieu, Y. Bréchet, Precipitates and boundaries interaction in ferritic ODS steels, J. Nucl. Mater. 472 (2016) 118–126, https://doi.org/10.1016/j.jnucmat.2016.01.021.
[77] P.M. Hazzledine, Direct versus indirect dispersion hardening, Scr. Metall. Et. Mater. 26 (1992) 57–58, https://doi.org/10.1016/0956-716X(92)90368-O.
[78] J.H. Schneibel, M. Heilmaier, Hall-Petch breakdown at elevated temperatures, Mater. Trans. 55 (2014) 44–51, https://doi.org/10.2320/matertrans.MA201309.
[79] N. Luptáková, D. Bártková, Pathways of development of oxide dispersion-strengthened alloys, Front. Mater. 12 (2025) 1690201, https://doi.org/10.3389/fmats.2025.1690201.
[80] R. Kocich, L. Kunčická, P. Král, K. Dvořák, Mechanical behavior of oxide dispersion strengthened steel directly consolidated by rotary swaging, Materials 17 (2024) 4831, https://doi.org/10.3390/ma17194831.
[81] M.K. Dash, H. Tripathy, S. Saroja, R. Mythili, Evaluation of deformation and recrystallization behavior in oxide dispersion strengthened 18Cr ferritic steel, Int. J. Press. Vessels Pip. 185 (2020) 104130, https://doi.org/10.1016/j.ijpvp.2020.104130.